*Desalination and Water Treatment*
www.deswater.com

doi: 10.5004/dwt.2023.29919

308 (2023) 150–159
October

# Synthesis of Z-scheme $Ag/AgI/Bi_2MoO_6$ nanocomposites used for high-efficiency visible-light-driven photocatalyst

Anukorn Phuruangrat[a,*], Kamonlak Suriyarpitak[a], Surangkana Wannapop[b], Titipun Thongtem[c,d], Somchai Thongtem[c,e,*]

[a]*Division of Physical Science, Faculty of Science, Prince of Songkla University, Hat Yai, Songkhla 90112, Thailand, Tel.: +66 (0)74 288374; Fax: +66 (0)74 288395; emails: phuruangrat@hotmail.com (A. Phuruangrat), 5710210007@psu.ac.th (K. Suriyarpitak)*
[b]*Faculty of Science, Energy and Environment, King Mongkut's University of Technology North Bangkok, Rayong Campus, Rayong 21120, Thailand, email: surangkana.w@sciee.kmutnb.ac.th*
[c]*Materials Science Research Center, Faculty of Science, Chiang Mai University, Chiang Mai 50200, Thailand, Tel.: +66 (0)53 941915; Fax: +66 (0)53 941915; emails: schthongtem@yahoo.com (S. Thongtem), ttpthongtem@yahoo.com (T. Thongtem)*
[d]*Department of Chemistry, Faculty of Science, Chiang Mai University, Chiang Mai 50200, Thailand*
[e]*Department of Physics and Materials Science, Faculty of Science, Chiang Mai University, Chiang Mai 50200, Thailand*

Received 29 September 2023; Accepted 21 August 2023

**ABSTRACT**

Visible-light-driven Z-scheme $Ag/AgI/Bi_2MoO_6$ photocatalysts were successfully prepared via precipitation–sonochemical deposition method. Structure, morphology, composition and optical properties of as-prepared Z-scheme $Ag/AgI/Bi_2MoO_6$ nanocomposites were characterized by X-ray diffraction, X-ray photoelectron spectroscopy, transmission electron microscopy, UV-Visible diffuse reflectance spectroscopy and photoluminescence analysis. Comparing among the $Bi_2MoO_6$, $AgI/Bi_2MoO_6$ and $Ag/AgI/Bi_2MoO_6$ samples, the Z-scheme $Ag/AgI/Bi_2MoO_6$ photocatalyst exhibited the enhanced photocatalytic performance for the degradation of Rhodamine B (RhB) under visible radiation due to the formation of heterostructure of Ag/AgI and $Bi_2MoO_6$. The trapping experiment certified that $h^+$ and $^{\bullet}O_2^-$ are the major active species in the photodegradation of RhB. The $Ag/AgI/Bi_2MoO_6$ nanocomposites have very high photostability and can be used for the photocatalytic application.

*Keywords:* Z-scheme photocatalyst; $Ag/AgI/Bi_2MoO_6$ nanocomposites; Spectroscopy

## 1. Introduction

In recent years, wastewater containing dyes of textile and printing industries are one of the important pollutants which have carcinogenic effect to human health even at low concentration [1–4]. Wastewater treatment using photocatalysts to remove dye contaminants in wastewater with the assistance of solar energy has attracted a great interest as an environmentally friendly technology because it is eco-friendly, low cost, easy operation, good stability and high efficiency [1,5–8]. The visible radiation containing about 43% of solar energy is able to induce photocatalysis which is the focus of this research [8–10].

$Bi_2MoO_6$ as an *n*-type semiconductor with narrow band gap (2.5–2.8 eV) is a typical Aurivillius-phase perovskite with unique layered structure of $[Bi_2O_2]^{2+}$ inserted in $[MoO_4]^{2-}$ slabs. It is a promising candidate for photocatalytic process and is enable to capture visible light due to its

* Corresponding authors.

intrinsic chemical inertness, non-toxic and excellent spectral characteristics [2,6,11,12]. Nevertheless, the rapid combination of exciton and poor quantum yield can lead to limit the photocatalytic performance of $Bi_2MoO_6$ [1,2,11,13,14]. Different approaches such as non-metal and metal doping [15–20] and coupling with other semiconductors (heterojunction) [1,2,6–8,11,13,14] were used to obtain the above issue. The most effective method in improving the photocatalytic performance of $Bi_2MoO_6$ is to form composites with Ag/AgX (X = Cl, Br and I) [5,21–24]. The noble metallic Ag can play the role in strong absorption in visible light region owing to the surface plasmon resonance (SPR) effect and improving electron transport [5,21,25,26]. When Ag nanoparticles incorporated with $Bi_2MoO_6$ semiconductor, they can perform functional ability of promoting interfacial charge–transfer due to their high Schottky barrier at the nanoparticle-semiconductor interface [11,21,26,27]. Meanwhile, AgX (X = Br Cl and I) photosensitive materials were demonstrated to be a class of efficient visible light responsive photocatalyst which can improve the separation efficiency of photo-generated charge carriers and enhance photocatalytic activity of the supporting photocatalyst [5,21,28]. Among them, AgI with the smallest band gap shows the most excellent application prospect in photocatalysis [21,29]. The Ag/AgI/$Bi_2MoO_6$ nanocomposites can play the role in enhancing the photocatalytic performance under visible light irradiation due to the incorporated SPR effect of metallic silver on the photosensitive AgI host and highly effective interfacial charge transfer between Ag/AgI and $Bi_2MoO_6$ [22,25,26,30].

In this work, Z-scheme Ag/AgI/$Bi_2MoO_6$ photocatalyst as visible-light-driven photocatalyst was successfully prepared by precipitation–sonochemical deposition method. The structure, morphology, composition and optical properties of as-prepared Z-scheme Ag/AgI/$Bi_2MoO_6$ nanocomposites were characterized by X-ray diffraction (XRD), transmission electron microscopy (TEM), X-ray photoelectron spectroscopy (XPS), diffuse reflectance UV-Visible spectroscopy (DRS), photoluminescence (PL) spectroscopy and Brunauer–Emmett–Teller (BET) surface area analysis. The photocatalytic activity of Z-scheme Ag/AgI/$Bi_2MoO_6$ photocatalyst was investigated through Rhodamine B (RhB) degradation under visible light irradiation. In addition, the photocatalytic stability and main active radical were further investigated for possible link between the photocatalytic material and RhB model dye.

## 2. Experiment

In this research, each of $Bi(NO_3)_3·5H_2O$ and $Na_2MoO_4$ was weighed and dissolved in 50 mL reverse osmosis (RO) water under continued stirring. Then, the two solutions were mixed together under continued stirring and the mixed solution was adjusted to pH 6 by 3 M NaOH. The mixed solution was transferred into a Teflon-lined autoclave and heated at the constant temperature of 180°C for 20 h in an electric oven. In the end, the precipitates were filtered, washed and dried for further preparing of AgI/$Bi_2MoO_6$ and Ag/AgI/$Bi_2MoO_6$ nanocomposites.

Heterostructure 5% AgI/$Bi_2MoO_6$ nanocomposites were prepared by precipitation deposition method. 5% $AgNO_3$ and NaI by weight were dissolved in 25 mL RO water with continued stirring. Then, 2.5 g $Bi_2MoO_6$ nanoplates were put in 50 mL RO water with continued stirring. The $AgNO_3$ and NaI solution was dropped to the $Bi_2MoO_6$ suspension with continued stirring. Then, the heterostructure 5% AgI/$Bi_2MoO_6$ precipitates were filtered, washed and dried for further preparing the Ag/AgI/$Bi_2MoO_6$ nanocomposites.

Heterostructure 5% Ag/AgI/$Bi_2MoO_6$ nanocomposites were prepared by sonochemical-assisted deposition method. 5% $AgNO_3$ by weight was dissolved in 50 mL ethylene glycol with continued stirring. Then, 2.5 g of the as-prepared heterostructure 5% AgI/$Bi_2MoO_6$ nanocomposites was put in 50 mL ethylene glycol with continued stirring for 30 min. The AgI/$Bi_2MoO_6$ solution was dispersed in ultrasonic bath into which the $AgNO_3$ solution was dropped. The system was irradiated by ultrasonic wave for 20 min. In the end, the 5% Ag/AgI/$Bi_2MoO_6$ precipitates were filtered, washed and dried for further characterization.

Phase and purity of the samples were analyzed by Philips X'Pert MPD X-ray diffractometer (XRD) (U.S.A) with Cu $K_\alpha$ radiation as an X-ray source in the 10°–60° range at a scanning rate of 0.02°/s. Fourier-transform infrared (FTIR) spectra of samples were analyzed on a Bruker Tensor 27 Fourier-transform infrared spectrometer (Canada) using KBr as a diluting agent. The morphology of the as-prepared samples was observed through transmission electron microscopy (JEOL JEM-2010 TEM, U.S.A.) at an operating voltage of 200 kV. The elemental composition and oxidation state of samples were investigated by an X-ray photoelectron spectrophotometer (XPS, Axis Ultra DLD, Kratos Analytical Ltd., U.S.A.) using monochromated Al $K_\alpha$ radiation at 1,486.6 eV and C 1s at 285.1 eV as the standard. The optical and photoluminescence properties of samples were analyzed by a UV-Visible diffuse reflectance spectroscopy (Shimadzu UV-2600 Spectrophotometer, U.S.A.) over 200–800 nm wavelength at room temperature and a PerkinElmer LS-50B photoluminescence spectrometer (Canada) at 200–700 nm using an excitation wavelength of 328 nm. BET analysis for specific surface area of samples was operated on a Micromeritics TriStar II 3020 analyzer (U.S.A.).

The photocatalytic activities of as-synthesized photocatalysts were monitored through RhB degradation under visible light irradiation. The 200 mg photocatalyst was suspended in 200 mL $10^{-5}$ M RhB solution and stirred in the dark for 30 min. Under visible light irradiation, 5 mL RhB solution was sampled from the photocatalytic reactor every 20 min and separated the photocatalyst by centrifugation. The solution was analyzed by a PerkinElmer Lambda 25 UV-Visible spectroscopic analyzer (Canada) at 554 nm wavelength. The decolorization efficiency was calculated by the equation.

$$\text{Photocatalytic efficiency}(\%) = \frac{A_o - A_t}{A_o} \times 100 \quad (1)$$

where $A_o$ is the concentration of RhB in the dark and $A_t$ is the concentration of RhB after light irradiation. The reusability of the Ag/AgI/$Bi_2MoO_6$ nanocomposites was investigated by the degradation of RhB at the same condition for five cycles. $TiO_2$ P25 from PlasmaChem GmbH (Berlin, Germany) with the particle size of 21 ± 5 nm was used as a reference. The mineralization of RhB over Ag/AgI/$Bi_2MoO_6$ analyzed by total organic carbon (TOC) was investigated by a total organic carbon Analytik Jena Multi N/C 3100 analyzer (U.S.A.). In the end, the degraded RhB solution over Ag/AgI/$Bi_2MoO_6$ was studied by direct mass spectrometry (MS) Trace GC Ultra/ISQ Thermo Scientific Spectrometer (U.S.A.) using a positive electrospray ionization ($ESI^+$) mode.

## 3. Results and discussion

Fig. 1 presents the XRD patterns of the as-prepared $Bi_2MoO_6$, AgI/$Bi_2MoO_6$ and Ag/AgI/$Bi_2MoO_6$ samples. XRD pattern of pure $Bi_2MoO_6$ sample shows the sharp diffraction peaks located at 10.92°, 23.57°, 28.32°, 32.63°, 33.18°, 36.12°, 47.14°, 55.52°, 56.32° and 58.49° which can be assigned to the (020), (111), (131), (002), (060), (151), (202), (133), (191) and (262) crystal planes of orthorhombic $Bi_2MoO_6$ structure (JCPDS no. 21-0102 [31]), respectively. They should be noted that the diffraction intensity of the (0b0) facet of pure $Bi_2MoO_6$ sample is higher than that of the standard. The (0b0) facet of $Bi_2MoO_6$ is highly exposed. There was the report that an internal static electric field distributed along the b axis of the $[Bi_2O_2]^{2+}$ and $[MoO_4]^{2-}$ layers of $Bi_2MoO_6$. More efficient separation of photogenerated electron–hole pairs was obtained and photocatalytic performance was enhanced [32–35]. Impurity diffraction peaks were not detected, indicating that the single phase of orthorhombic $Bi_2MoO_6$ structure was obtained by hydrothermal method. The XRD pattern of AgI/$Bi_2MoO_6$ sample shows the diffraction peaks similar to those of the pure $Bi_2MoO_6$ sample. The results suggest that the major phase of AgI/$Bi_2MoO_6$ sample is orthorhombic $Bi_2MoO_6$ structure. Additional diffraction peaks at 23.72° and 39.21° can be indexed to the (111) and (220) crystal planes of face center cubic (FCC) AgI structure (JCPDS no. 09-0399 [31]). The AgI/$Bi_2MoO_6$ nanocomposites were successfully prepared by the precipitation–deposition method. An additional characteristic weak diffraction peak located at 38.21° was detected in Ag/AgI/$Bi_2MoO_6$ nanocomposites which can be indexed to the (111) plane of FCC metallic Ag structure (JCPDS no. 04-0783 [31]). No other diffraction peaks were detected in the XRD pattern of Ag/AgI/$Bi_2MoO_6$ nanocomposites. They were suggested that no impurities formed during the synthesis of Ag/AgI/$Bi_2MoO_6$ nanocomposites by the precipitation–sonochemical deposition method. The introduction of Ag/AgI did not play the role in changing the phase of $Bi_2MoO_6$. Ag/AgI phases were probably adsorbed on the $Bi_2MoO_6$ sample instead of covalent incorporating in the crystal lattice of $Bi_2MoO_6$. The approximate crystallite sizes of Ag and AgI on Ag/AgI/$Bi_2MoO_6$ nanocomposites calculated by the Scherrer equation were 9.32 and 10.65 nm, respectively.

Fig. 2 shows FTIR spectra of as-prepared $Bi_2MoO_6$, AgI/$Bi_2MoO_6$ and Ag/AgI/$Bi_2MoO_6$ samples. The as-prepared $Bi_2MoO_6$ sample shows the FTIR bands at 950–400 $cm^{-1}$ which are related to the Bi–O stretching, Mo–O stretching and Mo–O–Mo bridging stretching modes [2,8,11,13,17]. The shoulder bands at 843 and 798 $cm^{-1}$ are assigned to the asymmetric and symmetric Mo–O stretching modes of $MoO_6$ involving vibration of oxygen atoms [2,8,11,13,17]. The dominant band at 736 $cm^{-1}$ can be attributed to the asymmetric stretching mode involving vibration of the equatorial oxygen atoms [2,8,11,13,17]. The small FTIR bands at 602 and 575 $cm^{-1}$ were detected in the as-prepared $Bi_2MoO_6$ sample and were assigned to the bending vibration of $MoO_6$ octahedrons [2,8,11,13,17]. Furthermore, the small FTIR band at 447 $cm^{-1}$ corresponds to the Bi–O stretching vibration of $BiO_6$ octahedron [1,2,11,13,17]. The FTIR spectra of AgI/$Bi_2MoO_6$ and Ag/AgI/$Bi_2MoO_6$ nanocomposites are similar to that of the pure $Bi_2MoO_6$ sample, indicating that the loaded AgI and Ag/AgI were supported on the $Bi_2MoO_6$ sample. The broad band at 3,200–3,400 $cm^{-1}$ was detected in all samples and corresponds to O–H stretching vibration of absorbed water on the top [2,13,17].

Fig. 3 shows the TEM and high-resolution transmission electron microscopy images, and Selected Area Electron Diffraction (SAED) pattern of $Bi_2MoO_6$, AgI/$Bi_2MoO_6$ and Ag/AgI/$Bi_2MoO_6$ nanocomposites. TEM image of $Bi_2MoO_6$ was composed of a large number of uniform $Bi_2MoO_6$ nanoplates with smooth surface. The average diameter of $Bi_2MoO_6$ nanoplates was 200–400 nm. SAED pattern of individual

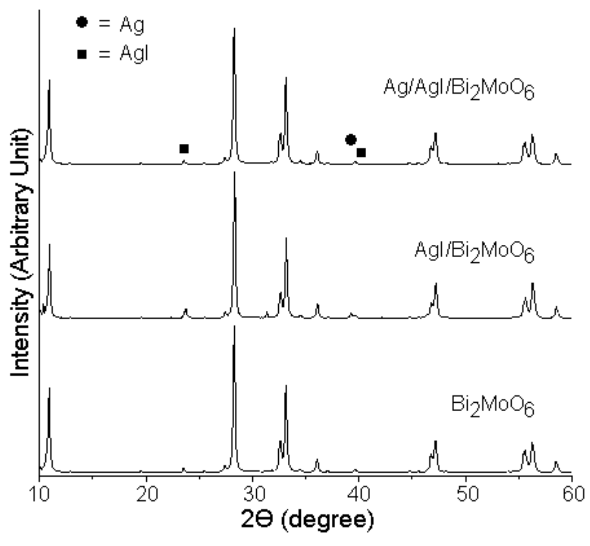


Fig. 1. X-ray diffraction patterns of the as-synthesized $Bi_2MoO_6$, AgI/$B_2MoO_6$ and Ag/AgI/$Bi_2MoO_6$ samples.

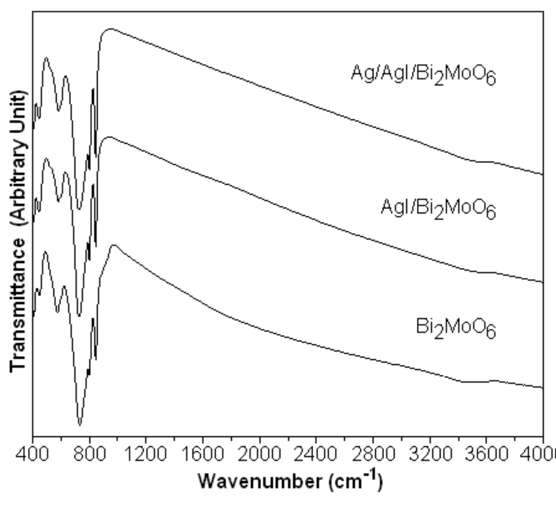


Fig. 2. Fourier-transform infrared spectra of the as-synthesized $Bi_2MoO_6$, AgI/$B_2MoO_6$ and Ag/AgI/$Bi_2MoO_6$ samples.

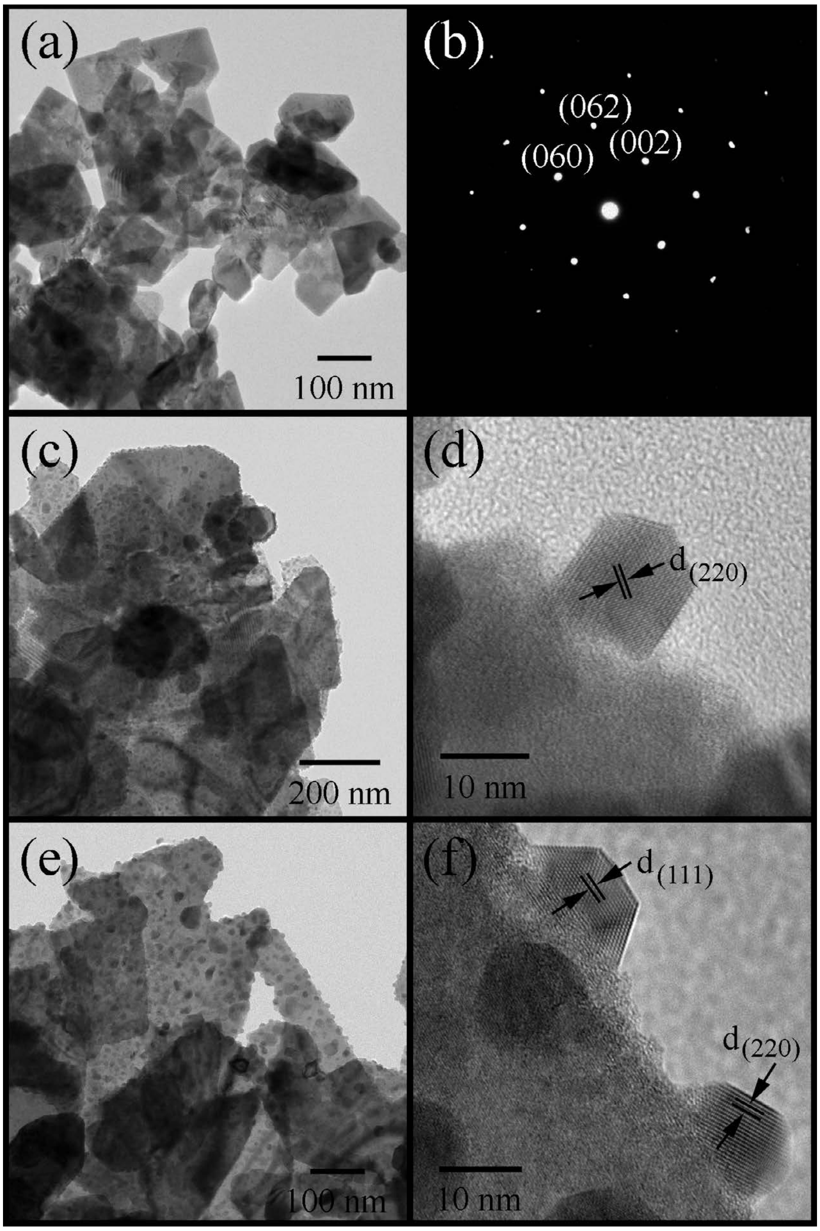


Fig. 3. Transmission electron microscopy images, SAED pattern and high-resolution transmission electron microscopy images of the as-synthesized (a,b) $Bi_2MoO_6$, (c,d) AgI/$Bi_2MoO_6$ and (e,f) Ag/AgI/$Bi_2MoO_6$ samples.

$Bi_2MoO_6$ nanoplate shows well-defined bright spots of electron diffraction of good single crystalline $Bi_2MoO_6$ phase. The SAED pattern of individual $Bi_2MoO_6$ nanoplate was indexed to the (060), (062) and (002) planes of orthorhombic $Bi_2MoO_6$ phase with zone axis of (100). The (100) surface is preferential orientation of orthorhombic $Bi_2MoO_6$ structure [17,19,36,37]. Meanwhile, the obtained AgI/$Bi_2MoO_6$ and Ag/AgI/$Bi_2MoO_6$ nanocomposites presented the numerous nanoparticles with the size of 15–20 nm decorated on the surface of $Bi_2MoO_6$ nanoplates, proving the formation of AgI/$Bi_2MoO_6$ and Ag/AgI/$Bi_2MoO_6$ heterojunctions, including the AgI/$Bi_2MoO_6$ and Ag/AgI/$Bi_2MoO_6$ interfaces. The formation of ternary Ag/AgI/$Bi_2MoO_6$ heterojunction played the role in enhancing the separation of photo-induced charge carriers and the photocatalytic performance. The (220) lattice plane with 0.232 nm apart of FCC AgI structure and (111) lattice plane with 0.236 nm apart of FCC Ag structure of Ag/AgI/$Bi_2MoO_6$ nanocomposites show that Ag/AgI nanoparticles were successfully loaded on top of $Bi_2MoO_6$ nanoplates.

The surface area of the catalyst is the key role for photocatalytic performance in enhancing the photocatalytic activity because of the abundant active sites for adsorbed pollutant molecules on top. The surface area of the as-prepared photocatalyst was studied through the BET analysis [1,6,12,16]. Fig. 4 shows the nitrogen adsorption–desorption isotherms of $Bi_2MoO_6$ and Ag/AgI/$Bi_2MoO_6$ nanocomposites. The BET analysis of $Bi_2MoO_6$ and Ag/AgI/$Bi_2MoO_6$ nanocomposites corresponds to the type-IV isotherm with

$H_3$ adsorption hysteresis according to the International Union of Pure and Applied Chemistry classification which indicates the presence of mesoporous material [12,38,39]. Moreover, the specific surface area of Ag/AgI/$Bi_2MoO_6$ is 8.82 $m^2/g$ which is 1.25 times of the pure $Bi_2MoO_6$ sample (7.05 $m^2/g$). These Ag/AgI/$Bi_2MoO_6$ nanocomposites have the benefit for photocatalytic application better than the $Bi_2MoO_6$ sample [6,12,16,38,39].

XPS was used to study composition and oxidation state of elements of the as-prepared Ag/AgI/$Bi_2MoO_6$ sample. Fig. 5a shows the XPS survey spectrum of the as-prepared Ag/AgI/$Bi_2MoO_6$ sample which is mainly composed of Ag, I, Bi, Mo, O and C. The C element could be attributed to the adventitious hydrocarbon from the XPS instrument itself. Fig. 5b shows the high-resolution asymmetric binding energy peaks of Ag 3d. The spectrum was further de-convoluted into four symmetric binding energy peaks at 368.19, 369.21, 374.17 and 374.95 eV. The binding energy peaks at 368.19 eV for Ag $3d_{5/2}$ and 374.17 eV for Ag $3d_{3/2}$ were assigned to $Ag^+$ species of AgI. Those located at 369.21 eV for Ag $3d_{5/2}$ and 374.95 eV for Ag $3d_{3/2}$ were assigned to metallic $Ag^0$. These show the existence of metallic $Ag^0$ and AgI containing in the nanocomposites [2,3,5,8,21,24,26,40]. The high-resolution binding energy peaks centered at 619.36 and 630.93 eV (Fig. 5c) correspond to I $3d_{5/2}$ and I $3d_{3/2}$ core level, indicating that $I^-$ species belong to AgI [5,20,21,26,40]. The two symmetric binding energy peaks centered at 159.22 and 164.54 eV (Fig. 5d) were belonging to Bi $4f_{7/2}$ and Bi $4f_{5/2}$ core levels, suggesting that the oxidation state of Bi in $Bi_2MoO_6$ was 3+ [1,2,7,8,17]. The Mo $3d_{5/2}$ and Mo $3d_{3/2}$ core levels of $Mo^{6+}$ (Fig. 5e) were detected at binding energies of 232.51 and 235.65 eV [1,2,7,8,17]. In addition, the asymmetric binding energies of O 1s core level as shown in Fig. 5f can be further de-convoluted into 529.44, 530.81, 531.87 and 532.95 eV which are related to the Bi–O and Mo–O bonds in $Bi_2MoO_6$ lattice and chemisorbed oxygen such as $OH^-$ and $H_2O$ on the surface of nanocomposites [1,2,7,8,17]. The XPS analysis demonstrates that Ag/AgI/$Bi_2MoO_6$ nanocomposites were successfully prepared by precipitation–sonochemical deposition method.

The optical properties of the as-prepared samples were investigated by UV-Visible diffuse reflectance spectra (DRS) as the results shown in Fig. 6. The DRS spectrum of pure $Bi_2MoO_6$ nanoplates shows the lowest absorption in the UV-Visible region with absorption edge of 480 nm due to

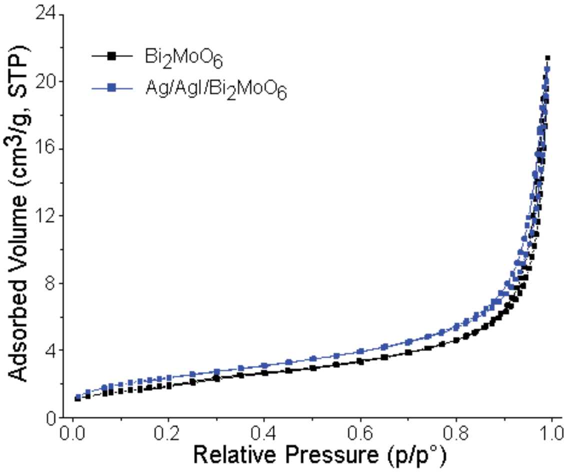


Fig. 4. Nitrogen adsorption–desorption isotherms of $Bi_2MoO_6$ and Ag/AgI/$Bi_2MoO_6$ samples.

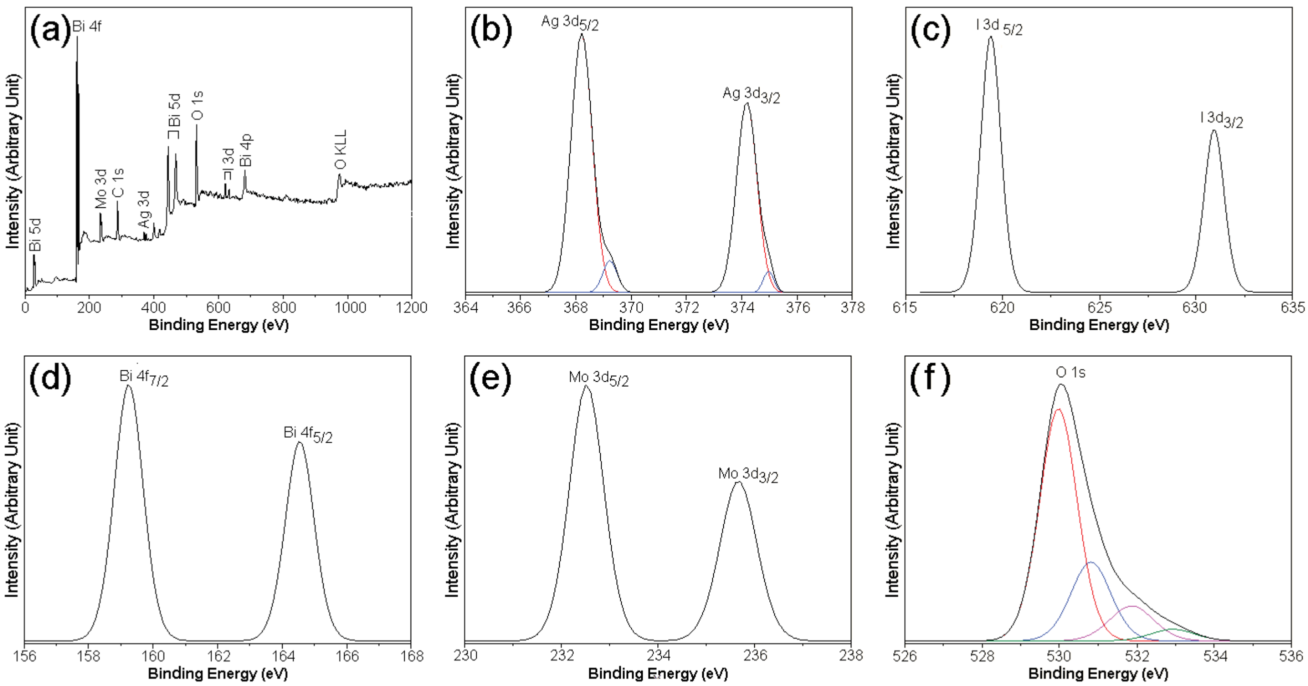


Fig. 5. (a) Survey X-ray photoelectron spectrum and high-resolution X-ray photoelectron spectra of (b) Ag 3d, (c) I 3d, (d) Bi 4f, (e) Mo 3d and (f) O 1s core levels of Ag/AgI/$Bi_2MoO_6$ sample.

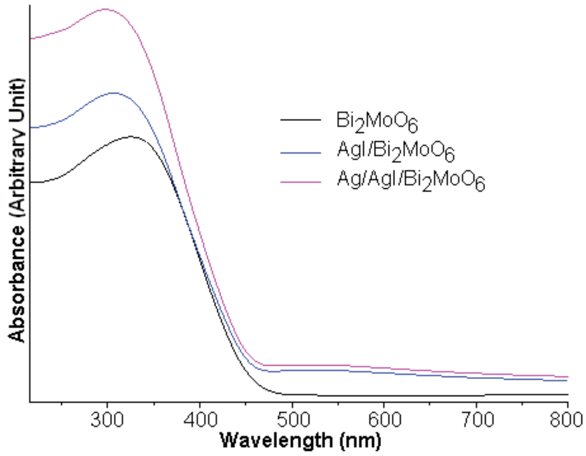


Fig. 6. UV-Visible diffuse reflectance spectra of $Bi_2MoO_6$, AgI/$Bi_2MoO_6$ and Ag/AgI/$Bi_2MoO_6$ samples.

the intrinsic band gap transition [6,8,12]. For the nanocomposites, they show the absorption in visible region due to the smaller band gap of AgI and SPR effect of Ag nanoparticles. The results can play the role in benefiting the generation of electron–hole pairs for photocatalytic activity [5,8,21,22,26,40]. The absorption edges of AgI/$Bi_2MoO_6$ and Ag/AgI/$Bi_2MoO_6$ nanocomposites were red-shifted to 483 and 495 nm, indicating the improvement of their visible light absorption capacity [5,8,21,22,26,40]. The relationship between the band gap ($E_g$) and the band edge absorption of a semiconductor material is $E_g = 1,240/\lambda_g$, where $\lambda_g$ is the absorption edge [41–43]. The calculated $E_g$ values of $Bi_2MoO_6$, AgI/$Bi_2MoO_6$ and Ag/AgI/$Bi_2MoO_6$ nanocomposites were 2.58, 2.57 and 2.51 eV, respectively. The $E_g$ of $Bi_2MoO_6$ was decreased when AgI nanoparticles and Ag/AgI nanoparticles were loaded on top. Thus, the visible light absorption capacity of AgI/$Bi_2MoO_6$ and Ag/AgI/$Bi_2MoO_6$ nanocomposites were improved, and the photogenerated electrons and holes during photocatalytic reaction were increased [5,8,21,22,26].

Photocatalytic activities of as-prepared samples were monitored by the degradation the RhB under visible light irradiation. Fig. 7 shows the temporal evolution of the UV-Visible absorption spectra during the degradation of RhB photocatalyzed by $Bi_2MoO_6$, AgI/$Bi_2MoO_6$ and Ag/AgI/$Bi_2MoO_6$ nanocomposites under visible radiation. The UV-Visible absorption of RhB over Ag/AgI/$Bi_2MoO_6$ nanocomposites shows the highest decreasing rate with increasing in the irradiation time. Thus, the Ag/AgI/$Bi_2MoO_6$ nanocomposites have the best photocatalytic performance. Clearly, the absorption wavelength at 554 nm was gradual hypochromic shift to 498 nm due to the N-deethylation of RhB to rhodamine during photocatalytic process [7,11,17,44].

To investigate the influence of Ag/AgI on photocatalytic activity, Ag/AgI/$Bi_2MoO_6$ nanocomposites were used to degrade RhB solution under visible light irradiation. Fig. 8a shows the photocatalytic efficiencies of $Bi_2MoO_6$, AgI/$Bi_2MoO_6$ and Ag/AgI/$Bi_2MoO_6$ samples under visible light irradiation w.r.t. $TiO_2$ P25 and the blank test. The photocatalytic activity of $TiO_2$ P25 is the lowest because of its wide band gap energy of ~3.2 eV [2,3,6]. The photodegradation of

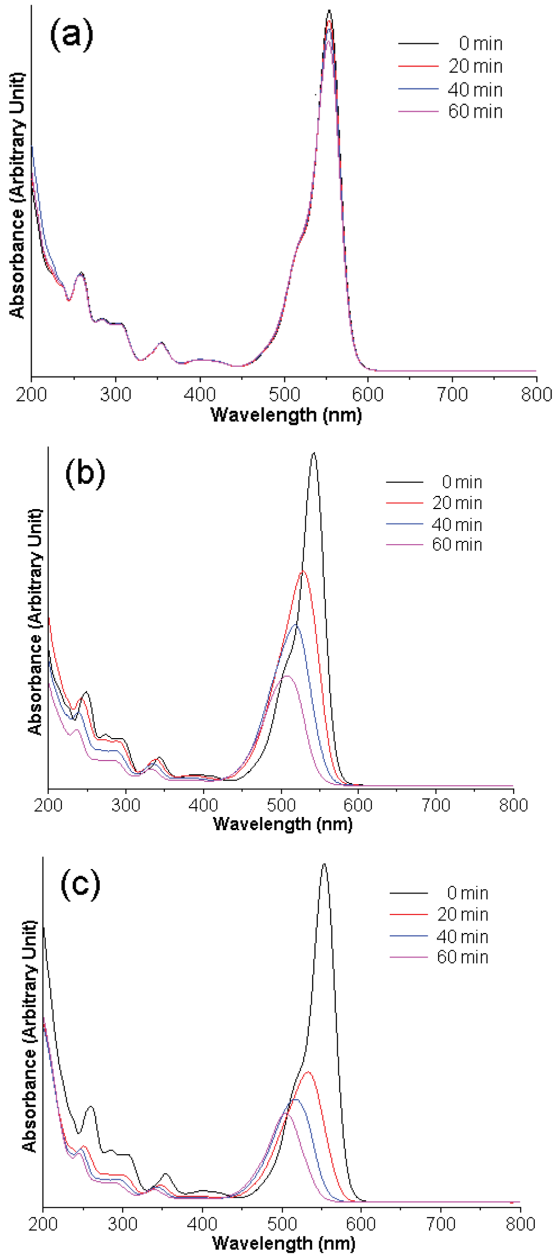


Fig. 7. UV-Visible absorption of Rhodamine B solutions photocatalyzed by (a) $Bi_2MoO_6$, (b) AgI/$Bi_2MoO_6$ and (c) Ag/AgI/$Bi_2MoO_6$ samples illuminated by visible radiation.

RhB over Ag/AgI/$Bi_2MoO_6$ nanocomposites was the highest. The introduction of Ag/AgI has the great influence on the photocatalytic activity. The photodegradation efficiencies were 8.94%, 92.81% and 98.67% for $Bi_2MoO_6$, AgI/$Bi_2MoO_6$ and Ag/AgI/$Bi_2MoO_6$ nanocomposites illuminated by visible radiation within 60 min, respectively. Moreover, the mineralization of RhB degradation was studied by TOC measurement. The mineralization percentages of RhB degradation by $Bi_2MoO_6$, AgI/$Bi_2MoO_6$ and Ag/AgI/$Bi_2MoO_6$ nanocomposites were 13.36%, 58.32% and 69.78%, respectively. The Ag/AgI/$Bi_2MoO_6$ nanocomposites have the highest photocatalytic performance caused by the synergistic effect of the formation Z-scheme of Ag/AgI and $Bi_2MoO_6$ heterojunctions due to the increase of active surface area and the strong visible light harvesting of the loaded Ag/AgI nanoparticles [5,7,8,21,22,26,30,40]. Photocatalytic reaction for the degradation of RhB follows the below pseudo-first-order kinetic model.

$$\ln\left(\frac{C_o}{C_t}\right) = kt \tag{2}$$

where $C_o$ and $C_t$ are the initial concentration and concentration at each specific reaction time ($t$) and $k$ is the kinetic reaction rate constant [7,8,17,18]. Fig. 8b shows the linear kinetic plots for $Bi_2MoO_6$, AgI/$Bi_2MoO_6$ and Ag/AgI/$Bi_2MoO_6$ nanocomposites illuminated by visible radiation w.r.t. $TiO_2$ P25 as a reference. The RhB degradation over photocatalysts follows pseudo-first-order kinetic model [7,8,12,17,18]. The kinetic rate constants were $5.64 \times 10^{-4}$, $2.10 \times 10^{-3}$, 0.0414 and 0.0737 for $TiO_2$ P25, $Bi_2MoO_6$, AgI/$Bi_2MoO_6$ and Ag/AgI/$Bi_2MoO_6$ samples, respectively. The Ag/AgI/$Bi_2MoO_6$ nanocomposites have the highest rate constant for the degradation of RhB under visible light irradiation owing to the formation of the ternary heterostructure between Ag/AgI and $Bi_2MoO_6$ [5,7,8,21,22,26,30,40]. To further investigate the enhanced photocatalytic property of the Ag/AgI/$Bi_2MoO_6$ heterojunction, PL spectroscopy was used to study the migration and separation of photo-induced carriers. The intensity of PL is related to the recombination of photo-induced carriers [1,2,6,12,21,26]. As displayed in Fig. 9, the PL spectrum of Ag/AgI/$Bi_2MoO_6$ heterojunction has the lowest intensity. The recombination of photo-induced carriers of $Bi_2MoO_6$ was suppressed by the loaded Ag/AgI. Thus, the photocatalytic performance of Ag/AgI/$Bi_2MoO_6$ heterojunction was the highest [1,3,6,12,21,26,40]. To study the degraded product photocatalyzed by Ag/AgI/$Bi_2MoO_6$, the RhB solution before and after photocatalytic reaction for a period of 60 min was analyzed by MS spectroscopy as the results shown in Fig. 10. Clearly, pure RhB molecules over Ag/AgI/$Bi_2MoO_6$ at $t = 0$ show the signal of $m/z = 443.3$, corresponding to the molecular weight of RhB. At the end of 60 min reaction, the $m/z$ at 443.3 was no longer detected because the RhB molecules were degraded by N-de-ethylation, chromophore cleavage, ring-opening and mineralization pathways. In the end, the generated intermediates were mineralized into $CO_2$ and $H_2O$ [45–47].

The recyclability and photostability of the photocatalyst are the important parameters for practical application. Thus, the recycled Ag/AgI/$Bi_2MoO_6$ nanocomposites were investigated for five cycled runs at the same condition. Fig. 11 shows the photocatalytic reaction of Ag/AgI/$Bi_2MoO_6$ nanocomposites for five recycles. The photodegradation of RhB over the Ag/AgI/$Bi_2MoO_6$ nanocomposites was only slightly reduced at the end of five recycled runs because the nanocomposites have very good stability against photo-corrosion under visible light. Thus, the Ag/AgI/$Bi_2MoO_6$ nanocomposites have very high photostability and photocatalytic activity for practical application. Moreover, the XRD analysis was used to investigate the crystal structure and phase of recycled Ag/AgI/$Bi_2MoO_6$ nanocomposites after five recycled runs as the results shown in Fig. 12. The XRD pattern of the used Ag/AgI/$Bi_2MoO_6$ nanocomposites was not changed during the photocatalytic reaction. There were no detection of additional peaks, therefore, the Ag/AgI/$Bi_2MoO_6$ nanocomposites are very stable crystal. In

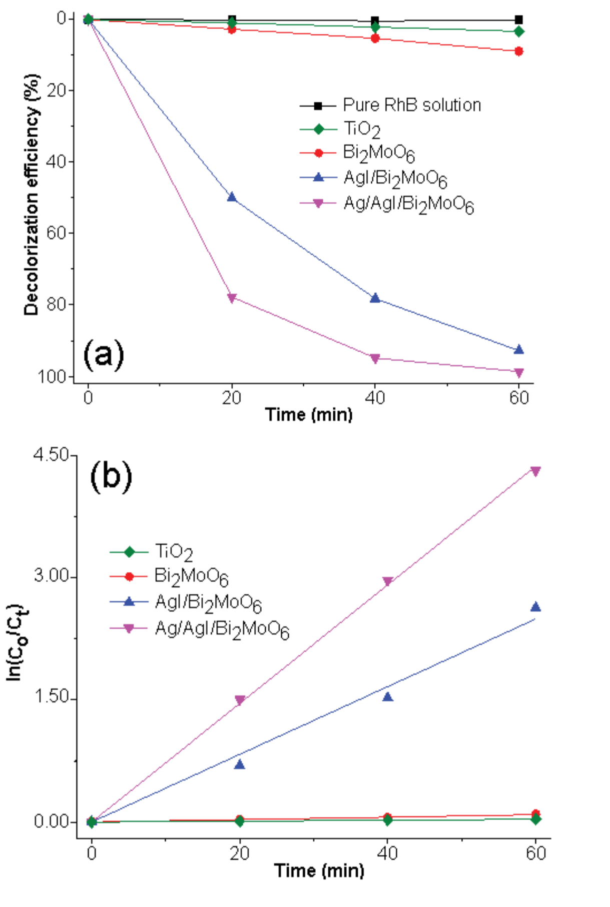


Fig. 8. (a) Decolorization efficiencies and (b) pseudo-first-order plots for the degradation of Rhodamine B solutions photocatalyzed by $Bi_2MoO_6$, AgI/$Bi_2MoO_6$ and Ag/AgI/$Bi_2MoO_6$ w.r.t. $TiO_2$ P25 and the blank test.

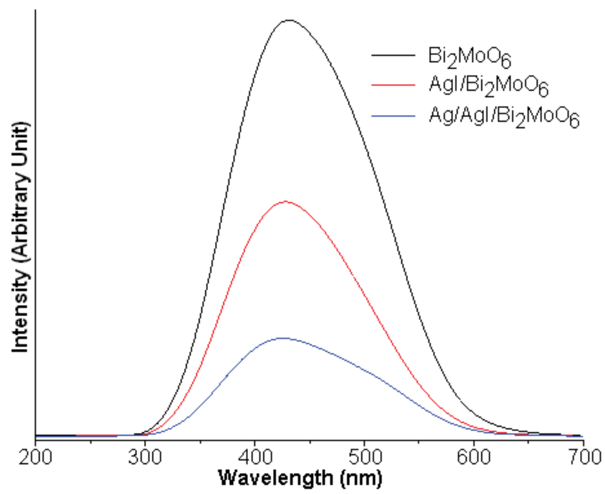


Fig. 9. Photoluminescence spectra of $Bi_2MoO_6$, AgI/$Bi_2MoO_6$ and Ag/AgI/$Bi_2MoO_6$ samples.

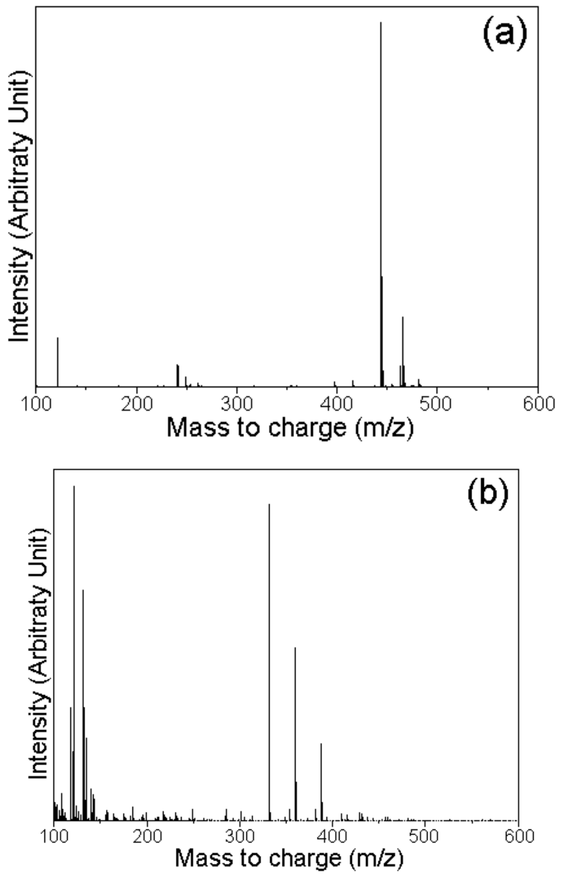


Fig. 10. Mass spectra of Rhodamine B (a) before and (b) after photocatalytic reaction of $Ag/AgI/Bi_2MoO_6$ nanocomposites for 60 min.

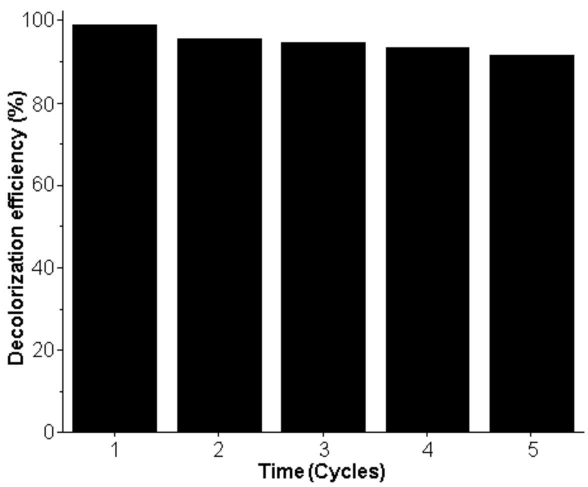


Fig. 11. Photocatalytic activities of reused $Ag/AgI/Bi_2MoO_6$ nanocomposites illuminated by visible radiation within five cycles.

other words, the ternary $Ag/AgI/Bi_2MoO_6$ heterojunction is a stable photocatalyst which can be utilized for photocatalytic activity in practical application.

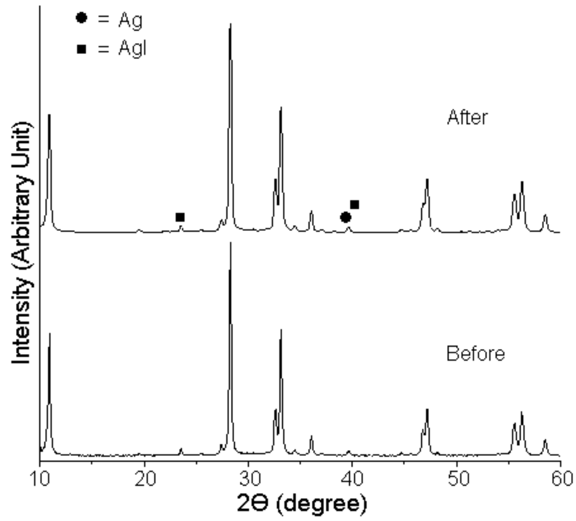


Fig. 12. X-ray diffraction patterns of $Ag/AgI/Bi_2MoO_6$ nanocomposites before and after photocatalytic test for five cycles.

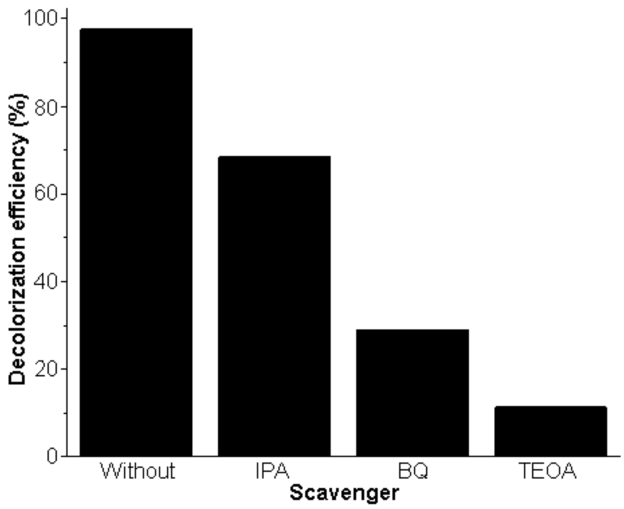


Fig. 13. Degradation of Rhodamine B solutions with and without scavengers over $Ag/AgI/Bi_2MoO_6$ nanocomposites.

In order to investigate the photocatalytic mechanism of RhB degradation over $Ag/AgI/Bi_2MoO_6$ nanocomposites under visible radiation, different active scavenger species such as triethanolamine (TEOA), benzoquinone (BQ) and isopropyl alcohol (IPA) for trapping of hole ($h^+$), superoxide ($^•O_2^-$) and hydroxyl ($^•OH$) radicals were added in the photocatalytic reaction, respectively [8,12,17,22,48,49]. Fig. 13 shows the influence of different active scavenger species on the photodegradation of RhB over $Ag/AgI/Bi_2MoO_6$ nanocomposites. Clearly, the photocatalytic efficiencies of $Ag/AgI/Bi_2MoO_6$ nanocomposites were drastically decreased from 98.67% to 11.35%, 28.95%, and 68.32% when TEOA, BQ and IPA were also added, respectively. Thus, $h^+$ and $^•O_2^-$ played the more important role in degrading of RhB photocatalyzed by $Ag/AgI/Bi_2MoO_6$ nanocomposites illuminated by visible radiation [8,22,50,51].

## 4. Conclusions

The visible-light-driven Z-scheme $Ag/AgI/Bi_2MoO_6$ photocatalysts were successfully prepared via precipitation–sonochemical deposition method. The analytical results certified that metallic Ag and AgI nanoparticles were decorated on the surface of orthorhombic $Bi_2MoO_6$ nanoplates. The Z-scheme $Ag/AgI/Bi_2MoO_6$ nanocomposites exhibited the highest degradation of Rhodamine B under visible light irradiation owing to the formation of the ternary heterostructure of Ag/AgI nanoparticles and $Bi_2MoO_6$ nanoplates. The trapping experiment showed that $h^+$ and $^{\bullet}O_2^-$ played the important role in the degradation process of RhB over $Ag/AgI/Bi_2MoO_6$ nanocomposites under visible radiation. The $Ag/AgI/Bi_2MoO_6$ nanocomposites exhibited very high photostability within five recycled runs and can be used for practical application.

## Declaration of competing interest

The authors declare that they have no known competing financial interests or personal relationships that could have appeared to influence the work reported in this paper.

## Acknowledgements

This research was supported by National Science, Research and Innovation Fund (NSRF), Thailand and Prince of Songkla University (Grant no. TAE6601072M).

## References

[1] M. Kasinathan, S. Thiripuranthagan, A. Sivakumar, Fabrication of 3D/2D $Bi_2MoO_6/g\text{-}C_3N_4$ heterostructure with enhanced photocatalytic behavior in the degradation of harmful organics, Emergent Mater., 4 (2021) 1363–1376.

[2] X. Liu, W.Y. Huang, Q. Zhou, X.R. Chen, K. Yang, D. Li, D.D. Dionysiou, Ag-decorated 3D flower-like $Bi_2MoO_6$/rGO with boosted photocatalytic performance for removal of organic pollutants, Rare Met., 40 (2021) 1086–1098.

[3] N.V.T. Thu, K.D. Dinh, Modification of $TiO_2$ with Ag nanoparticles using gamma irradiation method for photocatalytic degradation of azo dye, J. Aust. Ceram. Soc., 57 (2021) 1563–1570.

[4] A. Gulpiya, Z. Su, H. Pan, Hydrothermal synthesis of $Ag_2MoO_4$ with photocatalytic activity for Rhodamine B degradation, J. Aust. Ceram. Soc., 57 (2021) 91–96.

[5] B. Xu, Y. Li, Y. Gao, S. Liu, D. Lv, S. Zhao, H. Gao, G. Yang, N. Li, L. Ge, Ag-AgI/$Bi_3O_4Cl$ for efficient visible light photocatalytic degradation of methyl orange: the surface plasmon resonance effect of Ag and mechanism insight, Appl. Catal., B, 246 (2019) 140–148.

[6] S. Gu, Y. Zhang, X. Zhou, K. Sun, D. Wu, K. Gao, X. Wang, Bi–MO bimetallic Co-catalyst modified $Bi_2MoO_6$ for enhancing photocatalytic performance, J. Mater. Res., 36 (2021) 646–656.

[7] A. Phuruangrat, T. Klangnoi, P. Patiphatpanya, P. Dumrongrojthanath, S. Thongtem, T. Thongtem, Sonochemical-assisted deposition synthesis of visible-light-driven $Pd/Bi_2MoO_6$ used for photocatalytic degradation of Rhodamine B, J. Electron. Mater., 49 (2020) 3684–3691.

[8] R. Yang, Q. Zhao, B. Liu, Two-step method to prepare the direct Z-scheme heterojunction hierarchical flower-like Ag@AgBr/$Bi_2MoO_6$ microsphere photocatalysts for wastewater treatment under visible light, J. Mater. Sci., 31 (2020) 5054–5067.

[9] M. Urbonavicius, S. Varnagiris, S. Tuckute, Sa. Sakalauskaite, E. Demikyte, M. Lelis, Visible-light-driven photocatalytic inactivation of bacteria, bacteriophages, and their mixtures using ZnO-coated HDPE beads as floating photocatalyst, Materials, 15 (2022) 1318, doi: 10.3390/ma15041318.

[10] A. Upadhyaya, G. Rincón, Visible-light-active noble-metal photocatalysts for water disinfection: a review, Water Resour. Prot., 11 (2019) 1207–1232.

[11] P. Intaphong, P. Suebsom, A. Phuruangrat, K. Akhbari, S. Thongtem, T. Thongtem, Visible-light-driven 5% $Ag_{0.9}Pd_{0.1}/Bi_2MoO_6$ nanocomposites produced by photoreduction method, Russ. J. Inorg. Chem., 66 (2021) 1600–1607.

[12] C. Huang, S. Ma, Y. Zong, J. Gu, J. Xue, M. Wang, Microwave-assisted synthesis of 3D $Bi_2MoO_6$ microspheres with oxygen vacancies for enhanced visible-light photocatalytic activity, Photochem. Photobiol. Sci., 19 (2020) 1697–1706.

[13] J. Guo, R. Liu, Y. Ma, M. Wang, J. Li, X. Wei, L. Zhao, Synthesis and characterization of $SrFeO_{2.73}/Bi_2MoO_6$ heterojunction with enhanced photocatalytic activity, Catal. Lett., 151 (2021) 2176–2186.

[14] D. Li, P. Yan, Q. Zhao, X. Bai, X. Ma, J. Xue, Y. Zhang, M. Liu, Synthesis of $Bi_2WO_6/Bi_2MoO_6$ heterostructured nanosheet and activating peroxymonosulfate to enhance photocatalytic activity, J. Inorg. Organomet. Polym. Mater., 30 (2020) 5100–5107.

[15] X. Zhang, H. Zhang, H. Jiang, F. Yu, Z. Shang, Hydrothermal synthesis and characterization of $Ce^{3+}$ doped $Bi_2MoO_6$ for water treatment, Catal. Lett., 150 (2020) 159–169.

[16] Q. Wang, Z. Chen, M. Shi, Y. Zhao, J. Ye, G. He, Q. Meng, H. Chen, Zn-doped $Bi_2MoO_6$ supported on reduced graphene oxide with increased surface active sites for degradation of ciprofloxacin, Environ. Sci. Pollut. Res., 29 (2022) 19835–19846.

[17] A. Phuruangrat, S. Buapoon, T. Bunluesak, P. Suebsom, S. Thongtem, T. Thongtem, Degradation of Rhodamine B photocatalyzed by hydrothermally prepared Pd-doped $Bi_2MoO_6$ nanoplates, J. Aust. Ceram. Soc., 58 (2022) 71–82.

[18] D. Wang, H. Shen, L. Guo, C. Wang, F. Fu, Y. Liang, La and F co-doped $Bi_2MoO_6$ architectures with enhanced photocatalytic performance via synergistic effect, RSC Adv., 6 (2016) 71052–71060.

[19] A. Phuruangrat, P. Dumrongrojthanath, T. Thongtem, S. Thongtem, Hydrothermal synthesis and characterization of visible-light driven 0–3 wt.% Br-doped $Bi_2MoO_6$ photocatalysts, J. Ceram. Soc. Jpn., 125 (2017) 513–515.

[20] Z. Liu, X. Liu, C. Yu, L. Wei, H. Ji, Fabrication and characterization of I doped $Bi_2MoO_6$ microspheres with distinct performance for removing antibiotics and Cr(VI) under visible light illumination, Sep. Purif. Technol., 247 (2020) 116951, doi: 10.1016/j.seppur.2020.11695.

[21] C. Ding, K. Fu, Y. Pan, J. Liu, H. Deng, J. Shi, Comparison of Ag and AgI-modified ZnO as heterogeneous photocatalysts for simulated sunlight driven photodegradation of metronidazole, Catalysts, 10 (2020) 1097, doi: 10.3390/catal10091097.

[22] Y. Wang, C.G. Niu, L. Zhang, Y. Wang, H. Zhang, D.W. Huang, X.G. Zhang, L. Wang, G.M. Zeng, High-efficiency visible-light $AgI/Ag/Bi_2MoO_6$ as a Z-scheme photocatalyst for environmental applications, RSC Adv., 6 (2016) 10221–10228.

[23] S. Li, B. Xue, G. Wu, Y. Liu, H. Zhang, D. Ma, J. Zuo, A novel flower-like Ag/AgCl/BiOCOOH ternary heterojunction photocatalyst: facile construction and its superior photocatalytic performance for the removal of toxic pollutants, Nanomaterials, 9 (2019) 1562, doi: 10.3390/nano9111562.

[24] W. Gan, J. Zhang, H. Niu, L. Bao, H. Hao, Y. Yan, K. Wu, X. Fu, Fabrication of $Ag/AgBr/Bi_2WO_6$ hierarchical composites with high visible light photocatalytic activity, Chem. Phys. Lett., 737 (2019) 136830, doi: 10.1016/j.cplett.2019.136830.

[25] Y. Liang, H. Wang, L. Liu, P. Wu, W. Cui, J.G. McEvoy, Z. Zhang, Microwave-assisted synthesis of a superfine Ag/AgI photocatalyst with high activity and excellent durability, J. Mater. Sci., 50 (2015) 6935–6946.

[26] Z. Song, P. Lin, Z. Ma, F. Wang, G.S. Huang, Construction and characterization of $Ag/AgI/Ag_3BiO_3$ heterojunction and its photocatalytic mechanism, J. Exp. Nanosci., 14 (2019) 56–68.

[27] S. Buapoon, A. Phuruangrat, P. Dumrongrojthanath, T. Thongtem, S. Thongtem, Sonochemical synthesis and characterization of Ag/ZnO heterostructure nanocomposites

and their photocatalytic efficiencies, J. Electron. Mater., 50 (2021) 4524–4532.

[28] C. An, J. Wang, J. Liu, S. Wang, Q.H. Zhang, Plasmonic enhancement of photocatalysis over Ag incorporated AgI hollow nanostructures, RSC Adv., 4 (2014) 2409–2413.

[29] X. Ma, Y. Dai, M. Guo, B. Huang, The role of effective mass of carrier in the photocatalytic behavior of silver halide-based Ag@AgX (X = Cl, Br, I): a theoretical study, ChemPhysChem, 13 (2012) 2304–2309.

[30] D. Yu, J. Bai, H. Liang, J. Wang, C. Li, Fabrication of a novel visible-light-driven photocatalyst Ag-AgI-$TiO_2$ nanoparticles supported on carbon nanofibers, Appl. Surf. Sci., 349 (2015) 241–250.

[31] Powder Diffract. File, JCPDS-ICDD, 12 Campus Blvd, Newtown Square, PA 19073–3273, U.S.A., 2001.

[32] Y. Chen, W. Yang, S. Gao, L. Zhu, C. Sun, Q. Li, Internal polarization modulation in $Bi_2MoO_6$ for photocatalytic performance enhancement under visible-light illumination, ChemSusChem, 11 (2018) 1521–1532.

[33] R. Wang, D. Li, H. Wang, C. Liu, L. Xu, Preparation, characterization, and performance analysis of S-doped $Bi_2MoO_6$ nanosheets, Nanomaterials, 9 (2019) 1341, doi: 10.3390/nano9091341.

[34] H. Yu, L. Jiang, H. Wang, B. Huang, X. Yuan, J. Huang, J. Zhang, G. Zeng, Modulation of $Bi_2MoO_6$-based materials for photocatalytic water splitting and environmental application: a critical review, Small, 15 (2019) 1901008, doi: 10.1002/smll.201901008.

[35] C. Kongmark, V. Martis, C. Pirovano, A. Löfberg, W. Beek, G. Sankar, A. Rubbens, S. Cristol, R.N. Vannier, E. Bordes-Richard, Synthesis of γ-$Bi_2MoO_6$ catalyst studied by combined high-resolution powder diffraction, XANES and Raman spectroscopy, Catal. Today, 157 (2010) 257–262.

[36] Y. Zheng, F. Duan, J. Wu, L. Liu, M. Chen, Y. Xie, Enhanced photocatalytic activity of bismuth molybdates with the preferentially exposed {010} surface under visible light irradiation, J. Mol. Catal. A: Chem., 303 (2009) 9–14.

[37] X. Wu, Y.H. Ng, W.H. Saputera, X. Wen, Y. Du, S.X. Dou, R. Amal, J.A. Scott, The dependence of $Bi_2MoO_6$ photocatalytic water oxidation capability on crystal facet engineering, ChemPhotoChem, 3 (2019) 1246–1253.

[38] J. Bao, S. Guo, J. Gao, T. Hu, L. Yang, C. Liu, J. Peng, C. Jiang, Synthesis of $Ag_2CO_3/Bi_2WO_6$ heterojunctions with enhanced photocatalytic activity and cycling stability, RSC Adv., 5 (2015) 97195–97204.

[39] J. Li, X. Liu, L. Pan, W. Qin, Z. Sun, Enhanced visible light photocatalytic degradation of Rhodamine B by Bi/$Bi_2MoO_6$ hollow microsphere composites, RSC Adv., 4 (2014) 62387–62392.

[40] S. Lin, L. Liu, J. Hu, Y. Liang, W. Cui, Photocatalytic activity of Ag@AgI sensitized $K_2Ti_4O_9$ nanoparticles under visible light irradiation, J. Mol. Struct., 1081 (2015) 260–267.

[41] Z. Wu, X. He, Z. Gao, Y. Xue, X. Chen, L. Zhang, Synthesis and characterization of Ni-doped anatase $TiO_2$ loaded on magnetic activated carbon for rapidly removing triphenylmethane dyes, Environ. Sci. Pollut. Res., 28 (2021) 3475–3483.

[42] J. Wang, F. Meng, W. Xie, C. Gao, Y. Zha, D. Liu, P. Wang, $TiO_2$/$CeO_2$ composite catalysts: synthesis, characterization and mechanism analysis, Appl. Phys. A, 124 (2018) 645, doi: 10.1007/s00339-018-2027-1.

[43] Y. Zhou, D. Li, L. Yang, C. Li, Y. Liu, J. Lu, Y. Wang, Preparation of 3D urchin-like RGO/ZnO and its photocatalytic activity, J. Mater. Sci., 28 (2017) 7935–7942.

[44] P. Chen, Z. Zhang, S. Yang, Y. Yang, Y. Sun, Synthesis of BiOCl/$ZnMoO_4$ heterojunction with oxygen vacancy for enhanced photocatalytic activity, J. Mater. Sci., 32 (2021) 23189–23205.

[45] T. Liu, L. Wang, X. Lu, J. Fan, X. Cai, B. Gao, R. Miao, J. Wang, Y. Lv, Comparative study of the photocatalytic performance for the degradation of different dyes by $ZnIn_2S_4$: adsorption, active species, and pathways, RSC Adv., 7 (2017) 12292–12300.

[46] H. Yang, J. Yang, Photocatalytic degradation of Rhodamine B catalyzed by $TiO_2$ films on a capillary column, RSC Adv., 8 (2018) 11921–11929.

[47] Y. Zhang, Y. Ma, L. Wang, Q. Sun, F. Zhang, J. Shi, Facile one-step hydrothermal synthesis of noble metal-free hetero-structural ternary composites and their application in photocatalytic water purification, RSC Adv., 7 (2017) 50701–50712.

[48] S. Manikandan, D. Sasikumar, P. Maadeswaran, Synthesis, structural and optical properties of phosphorus doped $MnO_2$ nanorods as an under sunlight illumination with intensify photocatalytic for the degradation of organic dyes, Optik, 261 (2022) 169185, doi: 10.1016/j.ijleo.2022.169185.

[49] Y. Ma, C. Lv, J. Hou, S. Yuan, Y. Wang, P. Xu, G. Gao, J. Shi, 3D hollow hierarchical structures based on 1D BiOCl nanorods intersected with 2D $Bi_2WO_6$ nanosheets for efficient photocatalysis under visible light, Nanomaterials, 9 (2019) 322, doi: 10.3390/nano9030322.

[50] Q. Yan, M. Sun, T. Yan, M. Li, L. Yan, D. Wei, B. Du, Fabrication of a heterostructured Ag/AgCl/$Bi_2MoO_6$ plasmonic photocatalyst with efficient visible light activity towards dyes, RSC Adv., 5 (2015) 17245–17252.

[51] X. Li, S. Fang, L. Ge, C. Han, P. Qiu, W. Liu, Synthesis of flower-like Ag/AgCl-$Bi_2MoO_6$ plasmonic photocatalysts with enhanced visible-light photocatalytic performance, Appl. Catal., B, 176–177 (2015) 62–69.